Proceedings World Geothermal Congress 2020+1
Reykjavik, Iceland, April - October 2021

Permeability Anisotropy and Fluid Dispersion in Pervasively Fractured Lavas, Rotokawa Geothermal Field, New Zealand

Warwick M. Kissling and Cécile Massiot

1 Fairway Drive, Avalon, PO Box 30368, Lower Hutt 5040, New Zealand.

w.kissling@gns.cri.nz

Keywords: fracture flow, permeability anisotropy, fluid dispersion

ABSTRACT

In New Zealand's high temperature geothermal systems, fluids flow dominantly through fractured rocks with low matrix permeability. Although surface fault mapping and borehole image log data show numerous structures, it remains challenging to efficiently target permeable fractures in geothermal reservoirs. A common assumption is that the intersection of several fracture populations provides high connectivity, resulting in high permeabilities and increased dispersion of tracer particles. To test this assumption, we present fluid flow and tracer calculations in several distinct 2-D discrete fracture networks, each of which is broadly consistent with the fracture density and dip angle interpreted from borehole image logs in the Rotokawa Geothermal Field, a New Zealand andesite-hosted reservoir. There, fractures are dominantly steeply dipping (75°-90°) but with approximately 25% of fractures dipping between 30° and 70°. The population models we use for dip angle include single and paired normal distributions with different standard deviations, a mixed model with normal and uniform distributions, and an empirical distribution based directly on dip angle measurements. In all population models fracture lengths are calculated from a truncated power-law distribution, and apertures are set proportional to fracture length so that an overall fracture porosity of ~0.05 is maintained, as measured in thin sections, cores and borehole image logs.

Most models show pervasive connected fractures, with anisotropic flow and tracer transport dominantly parallel to the mean fracture dip. Permeability anisotropy increases as the standard deviation of the dip distribution decreases, with flow (and tracers particles) becoming increasingly channelled, until channels become separated and permeability drops. Models composed of two or three orientation sub-populations do not provide the expected increase in permeability compared to single-population models and have permeabilities similar to a single population model with a standard deviation of 15°. However, permeability anisotropy and tracer dispersion are higher for the models with several sub-populations than for single-population models with similar permeability. The spread in orientation in the Rotokawa data, rather than well-clustered individual fracture sets, is consistent with them being pervasively fractured lavas and allows a higher tracer dispersion than single tight populations. Strikingly, less than 4% of all fractures actively contribute to flow at the length scale of our model, 350 m, with the remainder occurring in isolated smaller groups which may store, rather than transport, fluids. In pervasively fractured rocks, the presence of multiple sub-populations of fracture orientation may thus not necessarily further enhance permeability at reservoir length scales.

1. INTRODUCTION

Fracture networks play an important role in many geothermal systems, where the rock matrix has low permeability and is therefore not able to support fluid flows necessary to sustain economic use of geothermal resources (Wilson and Rowland, 2016; Wood et al., 2001). Examples of such systems in New Zealand are the greywacke basement-hosted geothermal system at Kawerau (Milicich et al., 2016) and the andesitic lava-hosted system at Rotokawa (matrix permeability < 10^{-16} m^2, Siratovich et al., 2014; McNamara et al., 2015).

In geothermal systems where permeability is controlled by the matrix, or a mixture of matrix and fractures (e.g Wairakei, Tauhara, Mokai; Bignall et al., 2010) the behaviour of these reservoirs can be described by 'continuum' models. There, permeability and other rock properties are ascribed to computational model blocks of size on the order of 10-100 m, which are assumed to be constant within each block (e.g. Pruess, 1991). This continuum approach is not so satisfactory when the reservoir permeability is dominated by fractures. In this case, flows can be confined to much smaller 'fracture' length scales (say ≤ 1-10 m) while still extending over 'reservoir scale' distances (>100-1000 m) through a connected fracture system (Bonnet et al., 2001). In this situation, it is not possible to represent these structures with a normal continuum-type model without an impractically large number of model elements. An additional complication is that geological measurements of the geometry, permeability and other properties of fractures, e.g. by using borehole image logs, are not sufficient to fully constrain the properties of each fracture, let alone its connectivity with other fractures at reservoir scales. Indeed, while downhole measurements provide the *in-situ* measurements of the fracture systems, fracture information (location, orientation, thickness) is limited to the borehole, and the length of fractures are not known.

In this paper, we use fracture network statistics derived from downhole and core measurements of the Rotokawa geothermal system (Massiot et al., 2017a), and build on our earlier geometric modelling of fracture networks (Kissling and Massiot, 2017, 2018). We evaluate the effect of the variability of fracture orientation on the fracture network connectivity, permeability and fluid dispersion at reservoir length scales, which are of interest to reservoir engineers for improving reservoir management.

2. FRACTURE NETWORKS

2.1 Context and applicability

The calculations presented here represent the vertical flow through steeply-dipping fractures, as identified on borehole image logs of the Rotokawa geothermal system. The models and results are also equally applicable to horizontal flow through fracture systems

which have a dominant strike orientation (e.g. NE-SW observed throughout the Taupo Volcanic Zone (TVZ); Massiot et al., 2013; McNamara et al., 2017; Villamor et al., 2017a,b) and which also occur directly beneath impermeable layers (e.g. the Huka Falls Formation in the TVZ, and in other settings such as the Awibengkok geothermal system in Indonesia; Stimac et al., 2008).

2.2 Data and fracture network characterisation

Massiot et al (2017a) and Kissling and Massiot (2017) describe the basic data sources for the fracture system in andesitic formations at Rotokawa, the derivation of statistical properties of these networks and geometrical modelling/representation of them. This work quantified both the connectivity and tendency to form groups of fractures at reservoir scales, assuming a doubly-truncated power-law distribution for fracture length (Bonnet et al., 2001), and further deduced an optimal power-law exponent. A summary of the essential elements of this work is as follows:

- Image logs from three boreholes sampling >2 km of deviated borehole (average deviation ~20°) yield a linear fracture density (P10) of 0.55 ± 0.2 m^{-1}.
- Fracture lengths cannot be derived from borehole image logs, but they are assumed to follow a doubly- truncated power law distribution, where the range of fracture lengths is 20-100 m, with a 'best-fit' power-law exponent $\lambda = 2.0$.
- Fracture geometric aperture is set equal to fracture length/1000 for all fractures. This implies that the overall fracture porosity (including veins) is ~0.05, consistent with that observed in cores, thin-sections and image logs.
- Fracture centres are located in the model domain by choosing uniformly distributed random numbers in both X and Y directions.
- A model domain 350 m x 350 m x 100 m deep is used to represent fracturing on a reservoir scale
- Calculated flows are total volumetric flows through a 350 m x 100 m face of this rectangular block.

The geometric aperture of a fracture derived from borehole image logs or drill-cores is the distance between fracture or vein walls. However, image logs cannot differentiate between open, partially open and closed fractures (Massiot et al., 2017b). In addition, borehole image logs overestimate the geometrical fracture aperture at the borehole walls (Davatzes et al., 2010), and have a resolution (~5 mm) insufficient to detect most fractures observed on cores (<2 mm). Thus, the geometrical fracture aperture used in the models in this paper is significantly greater than the hydraulic aperture which controls the flow of fluids, as presented by e.g. Barton et al. (2013) and Masri et al. (2015). In this paper, we introduce an additional 'aperture factor' β, which converts from geometric to hydraulic aperture (see section 2.3).

At Rotokawa, most fractures are subvertical, dipping >70°, and statistical analysis of fracture strike and dip magnitude in the three boreholes revealed several populations of fractures with distinct distributions of dip magnitude (Massiot et al., 2017a). For simplicity, Kissling and Massiot (2017, 2018) represented the dips with a single normal probability distribution where the mean dip is vertical (90°) and the standard deviation 15°. In this study we use seven population models for fracture dip angle of varied complexity to explore the effects of dip magnitude variability on the ability of fracture networks to transport fluid. Figure 1 (and Table 1) shows the details of these distributions. Models 0,1,2 and 3 contain single populations of fractures with different variability about the same mean. Models 4 and 5 contain sub-populations with non-symmetric mean dip angles ($\mu \neq 90°$); here additional sub-populations with complementary mean dip angles (i.e. 180°-μ) but the same standard deviation σ have been added to symmetrize the distributions with respect to a 90° dip angle. The final model, model 6, is derived directly from measured borehole data which has been corrected for sampling biases (Terzaghi, 1965; Massiot et al., 2015) and is similarly symmetrized, with the fracture dips assigned into 10° wide bins between 0° and 180°. Each of these symmetrized fracture populations is referred to as a single sub-population in Figure 1 (and Table 1).

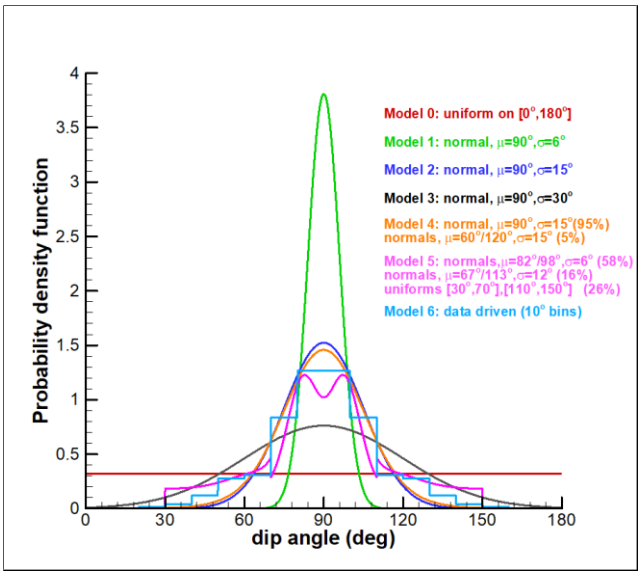

Figure 1: Probability density functions for fracture dip angle, for the seven models discussed in this paper. Models 2, 4, 5 resemble the observed fracture dip angles at the Rotokawa geothermal system in New Zealand (model 6), and models 0, 1 and 3 are used for comparison, and to illustrate some generic features of the flow through the fracture networks.

Table 1. Summary of flows and derived quantities for the fracture networks. In each column the square brackets [a,b] indicate the range of the quantity, and are followed by the mean ± 1 standard deviation.

Model	Orientation probability density function	Flow along-dip (Y direction) (m^3s^{-1} x 1000)	Flow across-dip (X direction) (m^3s^{-1} x 1000)	Permeability anisotropy (across/along)	Dispersion (m at 350 m)
0	Uniform between [0°, 180°]	[0.89,1.53], 1.21±0.23	[0.81,1.33], 1.11±0.17	[0.78,1.49], 1.10±0.18	[121,324], 263±64
1	Normal μ=90°, σ=6°	[0.024,0.61],0.35±0.18	[0,0.024],0.007±0.009	[20, Infinity]	[0,61]
2	Normal 90°, 15°	[2.25,3.79], 3.13±0.52	[0.14,0.36], 0.24±0.06	[10.4-24.5], 13.6±4.5	[45-144], 99±37
3	Normal 90°, 30°	[2.23,3.37], 2.70±0.34	[0.52,0.95], 0.74±0.15	[2.9-4.9], 3.7±0.7	[115-232], 178±37
4	2xNormal: • 90°, 15° (95%) • 60°/120°, 15° (5%)	[2.21,3.91], 3.12±0.51	[0.15,0.38], 0.28±0.08	[8.0-22.0], 12.0±4.0	[69-161], 116± 33
5	2xNormal: • 82°/98°, 6° (58%) • 67°/113°, 12° (16%) 1x uniform • [30°,70°]/[110°,150°] (26%)	[1.53,2.90], 2.35±0.46	[0.37,0.78], 0.50±0.12	[3.2-6.5], 4.8 ±1.1	[130-250], 182 ± 48
6	Data	[2.23,3.67], 2.93±0.48	[0.25,0.57], 0.37±0.08	[6.1-11.6], 8.2±1.7	[95-198], 144± 33

2.3 Modelling approach – algorithm and example results using a uniform distribution for fracture dip magnitude

In this section, we describe the modelling approach used in this paper, using 'model 0' as an example. The fracture network is constructed by sampling from probability distributions for fracture (centre) position, fracture length and fracture dip as shown in section 2.2. Fractures are added to the model until some measure of fracture density is reached (in this paper, P10 = 0.55 ± 0.2 m^{-1}). As the density of the network increases, the fractures form into groups, which ultimately control the permeability of the model domain. Figure 2a shows a network, for model 0, which has the specified linear fracture density and forms a single group (red fractures) which connects the entire model domain.

Typically, with the truncated power law distribution for fracture length, many of the shorter fractures remain unconnected within the network and so cannot contribute to the flow across the model domain (grey fractures, Figures 2a and 2b). Similarly, fractures which are connected to only one other (and not to the boundary) are unable to contribute to the overall flow (e.g., circled in Figure 2a and more clearly in 2b). These unconnected or singly-connected fractures are removed before the calculation of flow across the model can proceed. This process is iterative, and results in what is termed the 'backbone network' (or 'backbone' for short, Figure 2c), which is the subset of the original network (hereafter the 'full network') which can support flow across the model domain. The backbone network can contain voids, where there is a paucity of connected fractures (Figure 2a, with close-up view in Figure 2b), or regions of enhanced fracturing.

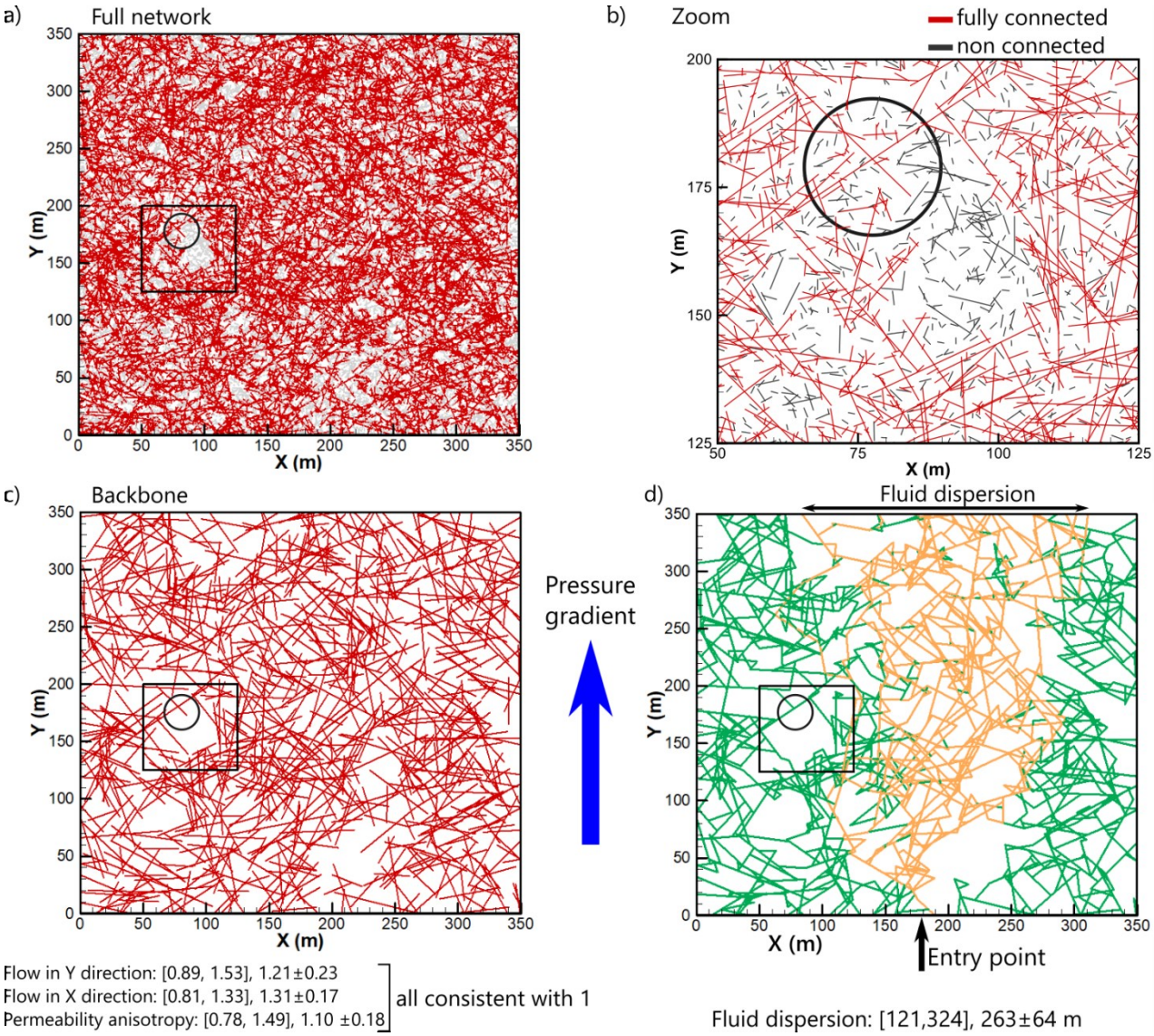

Figure 2:Example of fluid flow simulation through a DFN with uniform fracture orientation (model 0). a) Full network reproducing fracture density measured in borehole image logs. b) 75x75m zoom (square in panel 2a) showing fractures connected (red) and not connected (grey) to the backbone network. c) The backbone network used for flow simulations with a 1 bar pressure difference applied over the Y dimension of the model. Volumetric flows in the X and Y directions and permeability anisotropy all consistent with one. The circle encloses an example of a "dead-end" fracture which is stripped out for the fluid dispersion simulations. d) Example of fluid dispersion in a fracture network. The orange fractures trace the paths of 1000 fluid particles, propagated through the model as described in section 2.3. All of these particles enter the lower boundary through a single fracture ("entry point") but exit the model domain through several fractures across approximately 200 m at the upper boundary. The backbone network in panel 2d does not show the dead-end fracture segments because these do not contribute to the overall flow across the model. The figures below panels 2c and 2d report quantities derived from ten simulations in the format: [minimum, maximum], mean ± 1 standard deviation.

The backbone network (or equivalently each of its constituent fully-connected groups if there are more than one) describes the essential connectivity of the fracture network – the locations of all fracture intersections and the properties of the fracture segments connecting them. Locally, the calculation of fluid flow through the fracture system involves calculation of flows in these fracture segments. To do this, two things are required: a) a description of the length, hydraulic aperture and other physical properties of each fracture which govern the flow through it, and b) a mathematical flow law, from which the flow in the fracture segment can be calculated. In this paper we use the cubic flow law, which was first proposed by Boussinesq (1868) in a study of flow between smooth-sided parallel plates. A more recent review is contained in Zimmerman and Bodvarsson (1994). In this model the total volume flow of fluid in a single fracture, Q_{frac}, is proportional to the product of the cube of the hydraulic aperture of the fracture and the pressure gradient along it. The form of the cubic relation we use in this paper is

$$Q_{frac} = -(1/12\mu)\, H\, (\beta h)^3 dP/dL, \quad (1)$$

where μ is the dynamic viscosity of the fluid (in this paper calculated for water at 320 °C), H is the aquifer thickness out of plane, h is the geometric aperture of the fracture and dP/dL is the pressure gradient in the fracture segment. The 'aperture factor' β is the ratio of the hydraulic aperture to the geometric aperture and $(\beta h)^2/12$ is interpreted as the permeability of the fracture. In this paper we set

$\beta = 0.002$, a value derived to give a reservoir permeability of 10^{-13} m^2 for pervasively fractured rock at Rotokawa geothermal field (Kissling and Massiot, 2017). Other flow laws are possible (e.g. Klimczak et al., 2010; Liu et al., 2016,) which include other physical processes such as friction due to surface roughness and inertial effects. Though many of these retain the linear dependence of the flow on the pressure gradient, they are non-linear in the flowrate Q_{frac} and so require a different solution technique to that presented in this paper.

On a global 'reservoir' scale, the pressure distribution throughout the fracture network determines the flows in each fracture segment. The pressure field is the unknown quantity in the model and is represented by the pressure at each fracture intersection. Conservation of fluid mass (or equivalently volume, as the model is isothermal) at each fracture intersection (the sum of all ingoing and outgoing flows must be zero) leads to a linear equation involving the pressures at that intersection and its closest neighbours. The complete set of these equations yields a sparse matrix with a structure which depends on the connectivity of the backbone network, and a 'right hand side' formed from the known boundary pressures. This system can be readily solved for the pressures at all fracture intersections and consequently flows through the model domain are calculated by the summing flows for all fracture segments which cross each boundary.

For the networks described in this paper, flows through the fracture system were calculated by applying a pressure gradient from bottom (Y=0 m) to top (Y=350 m) across the model domain (Figure 2a). The pressure was set at nodes on the left and right boundaries by linear interpolation between the lower and upper boundary pressures. With these boundary conditions, the general direction of flow in the model domain will be parallel to the Y axis in the Figures and there are sufficient equations to give a unique solution for the pressure at each intersection.

Once the pressures have been calculated, the flows in each fracture segment are known, and can be used to trace the paths that fluid takes through the network (Figure 2d). This again is a probabilistic exercise. In this paper, we use the concept of tracer particle in the sense of fluid particles transported along the flow paths through the network. Inert chemical tracers of infinite dilution would behave in the same way. Figure 3 shows the three possible cases that can arise where a fluid 'tracer particle' reaches a fractures intersection.

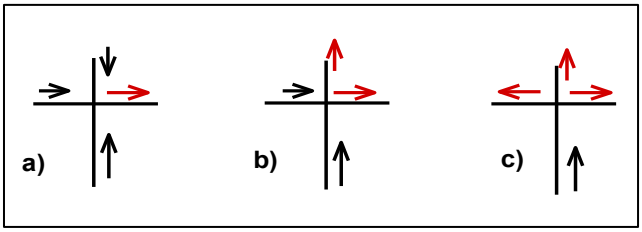

Figure 3: Possible fluid pathways when fluid reaches the intersection of two fractures (horizontal and vertical lines). Black arrows represent inflows to the intersection and the red arrows outflows. For any fluid entering the intersection, the probability of it leaving by any 'outflow' pathway is proportional to the flow in that pathway.

In panel (3a), inward flows of fluid occur from the top, the bottom, and from the left, and the single outflow is to the right. Because fluid mass is conserved at the intersection, the outflow is equal to the sum of the three inflows and any fluid entering the intersection has a 100% chance of taking the single outflow fracture. In panel (3b) there are two inflows and two outflows. Assuming all fluid entering the intersection is completely mixed, the probability of it leaving by one of the two exit fractures is simply proportional to the magnitude of the outflow in that fracture. In this way, the tracer particles can be propagated through the intersection, and on to the next one, by choosing an outflow path at each intersection which is consistent with this rule. In panel (3c) there are three outflows and a single inflow. The exit path is chosen in the same way according to the relative magnitudes of the three outflows. The procedure of tracking a tracer particle from one fracture intersection to the next is repeated until it reaches the top, lower pressure boundary of the modelled domain.

Figure 2d shows an example of this calculation for model 0. The orange fracture segments indicate the paths of 1000 fluid tracer particles which enter the model through a single fracture on the lower boundary of the model. This clearly shows that the fluid is dispersed in the network as it flows toward the upper boundary. In this paper we use the spread of tracer particles at the upper boundary (about 200 m in Figure 2d) as a measure of the ability of a given fracture network to disperse fluid.

2.4 Simulations

As the geometric properties of individual fracture networks are generated stochastically we run ten separate 'realisations' for each of the seven models shown in Figure 1. These are used to explore the variability of permeability (in two directions), permeability anisotropy and fluid dispersion both between and within each of the models. While this number of realisations is limited, it yields sufficiently well-defined means of quantities such as flows to allow comparison between the models while still providing useful insight in the inherent variability of these quantities.

3. RESULTS

3.1 How many fractures contribute to permeability?

Only a few percent of the total fracture population form part of the backbone and contribute to permeability (Figure 4). Remarkably, this proportion is the same for all models (3.7%) except model 1 where it ranges between 0.6% and 2.2%. The significance of this constant proportion is that fractures in models 2-6 provide continuous fully-connected paths enabling flow across the model domain in both the X and Y directions (we will use the term 'fully-connected' in this sense throughout this paper). The algorithm for creating the backbone network (section 2.3) always preserves this property of a fracture network. A similar ratio also occurs for model 0 (uniform distribution of dips), though there are fewer fractures in this case. The reduced number of fractures required to reach the

target linear density in this model is due to the greater probability of high-angle fractures intersecting the deviated boreholes (see first item in list in section 2.2), compared to other models where the fractures are, on average, at lower angles to the borehole.

All realisations of models 0, and 2-6 have just a single connected group throughout the model domain (as in Figure 2). In contrast, the realisations of model 1 yield backbones composed of up to six distinct connected groups, because the narrow dip distribution (6°) restricts the orthogonal 'reach' of the fractures and hence limits the horizontal connectivity (see Figure 6 for an example with six fully-connected groups). As a result, the number of fractures in the model 1 backbone is lower, and has a wider range, than in the other models (Figure 4). The minimum number (231 fractures) occurs in one realisation of model 1 where there is just one fully-connected group of fractures while the maximum number (1045 fractures) occurs when there are five fully-connected groups. The low proportion of fractures contributing to the backbone in model 1thus reflects the low connectivity in the X direction across this model.

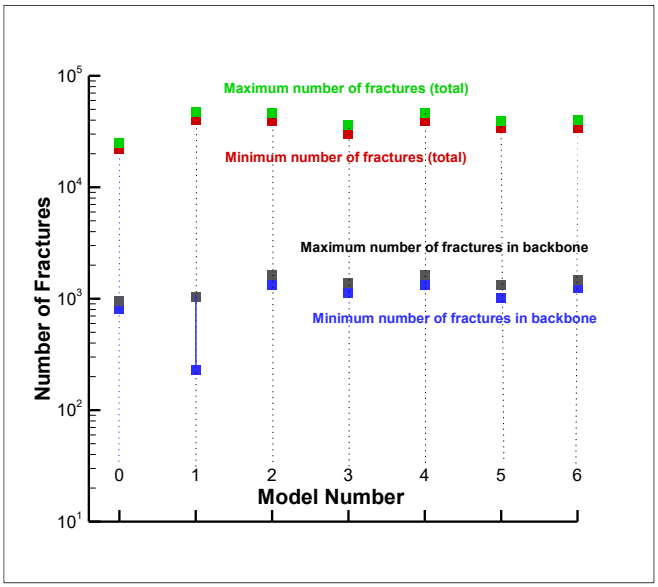

Figure 4. Numbers of fractures in full and backbone networks for each model. Note the logarithmic scale on the vertical axis. The number of fractures in the backbone network compared to those in the full network is remarkably constant at 3.7% for all models except model 1.

3.2 Permeability, permeability anisotropy and channelling

A basic property of a fracture network is its permeability. By using a Darcy-like flow law like equation (1) and the algorithm for calculating flows through the fracture network, a measure of the equivalent permeability in each direction through the network can be obtained. Results of these calculations for the seven models are shown in Figure 5a. The most obvious feature is the clustering of models 2 to 6, with models 0 and 1 being clear outliers. The latter two models have the largest and smallest variability in fracture dip of all our models – so large for model 0 that it has the largest across dip flow of all the models, and so small for model 1 that there is no across-dip flow in any of the 10 realisations of this model. Less obviously, the across-dip flow/permeability increases successively with the standard deviation of fracture dip in models 0, 1, 2, and 3. In turn, the along-dip permeability decreases in these models as the standard deviation of fracture dip increases. Overall, for all models, the dispersion of fluid decreases as the permeability becomes more anisotropic (Figure 5b).

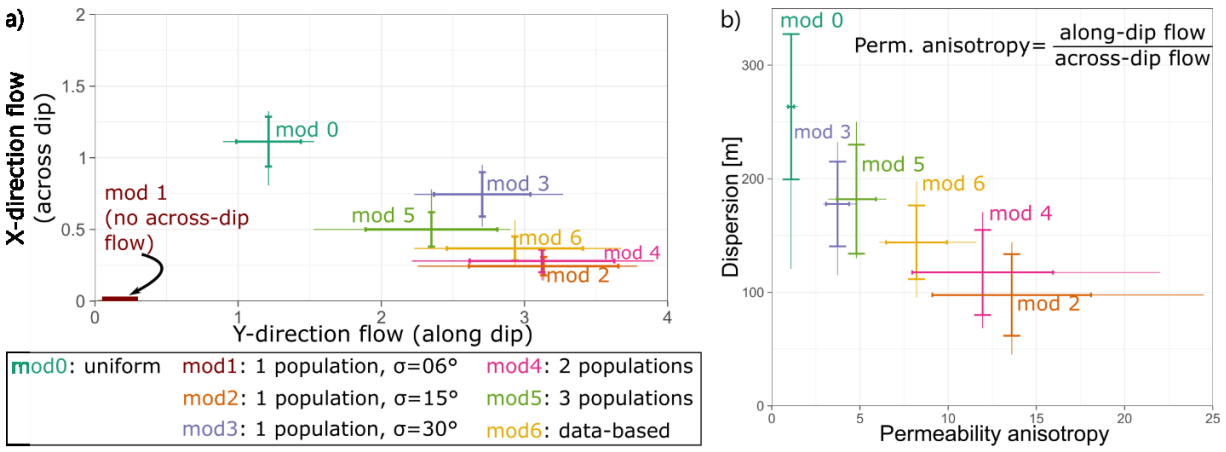

Figure 5. Summary statistics of the DFN. a) Across-dip (X direction) versus along-dip (Y direction) flow. b) Fluid dispersion versus permeability anisotropy. Note the broad 'inverse' relationship between fluid dispersion and permeability anisotropy.

Model 1 marks a tipping point between models where the backbone network is fully connected in both directions across the domain (fracture dip standard deviation >6°, as in Figure 2c), and models where fractures clump into distinct unconnected groups because the standard deviation of the fracture dips is too small (fracture dip standard deviation <6°, Figure 6) to provide connectivity in the X direction. This results in (a) fluids only being able to circulate in the Y direction (implying infinite permeability anisotropy), and (b) a strong channelling of fluids in the Y direction. In the realisation of model 1 presented in Figure 6 the colours indicate distinct unconnected groups of fractures, and the grey indicates background fracturing which does not provide connected permeability across the model. Because each of the six groups connect the upper and lower boundaries of the model there is some permeability in the Y direction, although this is lower than in other models because the backbone network contains fewer fractures.

Of the two models which have more than one sub-population of fracture orientation, model 4 has the most similar fracture dip distribution to the single-population model 2. The difference is that in model 4 five percent of the fractures are replaced by a population with a mean dip of 60°. For these two models, the means of the flows in each direction are extremely consistent, and though the permeability anisotropy and dispersion lie within one standard deviation of each other (Table 1) they do follow the clear inverse relationship indicated in Figure 5b. Model 5, which contains three sub-populations of fractures, shows along-dip flows reduced by ~25% compared to models 2 and 4, but almost double across-dip flow. The reduced permeability anisotropy (4.8) is consistent with the presence of more X-direction connectivity and the higher dispersion for this model.

Model 6, shows X and Y flows intermediate between the 'high flow' models 2 and 4 and the 'low-flow' model 5, and the derived quantities of permeability anisotropy and dispersion are consistent with the broad inverse trend shown in Figure 5b. This suggests that connectivity provided by the tails of this distribution (the high dip-angle fractures, close to 0° and 180°) in this data-driven model is greater than that provided by the single extra population in model 4, but less than that from the three-population model 5.

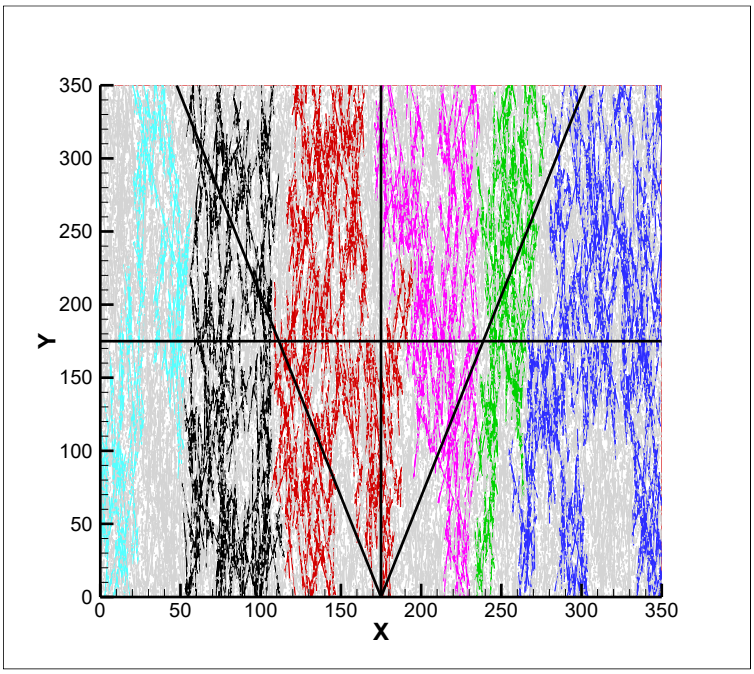

Figure 6: Distinct fracture groups in model 1 (normal dips, μ=90°, σ=6°). Colours indicate distinct unconnected groups of fractures. Grey indicates 'background' fracturing which does not provide connected permeability across the model, i.e. the groups comprise mainly short fractures which are only 'locally' connected. This provides good permeability in the Y direction (though reduced compared to the other models which are connected across the domain), but zero permeability in the X direction.

3.3 Fluid dispersion at reservoir scales.

For all models the connectivity of the fracture network yields an appreciable dispersion: fluids that enter the system at a single fracture can exit over a ~100 m-wide region after passing through the model domain (Figure 7a). If the mean fracture orientation is perpendicular to the pressure gradient (as might be the case locally in a geothermal reservoir, or if there is a population of fractures inherited from a previous deformation event), then the fluids sweep an even larger portion of the domain, and the dispersion is very high (Figure 7b).

As noted in section 3.3, the dispersion of fluid decreases as the permeability becomes more anisotropic (Figure 5b). The largest dispersion occurs for model 0, with a uniform distribution of dip angles, and the lowest for model 1, where the small standard deviation of the fracture dip angle results in the formation of distinct parallel 'channels' which lack X-direction connectivity (Figure 6). In this case, the dispersion is physically limited by the lateral extent of the channels. Models 4 (two populations) and 6 (data-driven) follow this trend and have dispersion intermediate between the single-population models 2 and 3 which have dips with 15° and 30° standard deviation. Model 5 (three populations) is similar to model 3, where the presence of more fractures in the tail of both distributions results in low permeability anisotropy and correspondingly greater fluid dispersion.

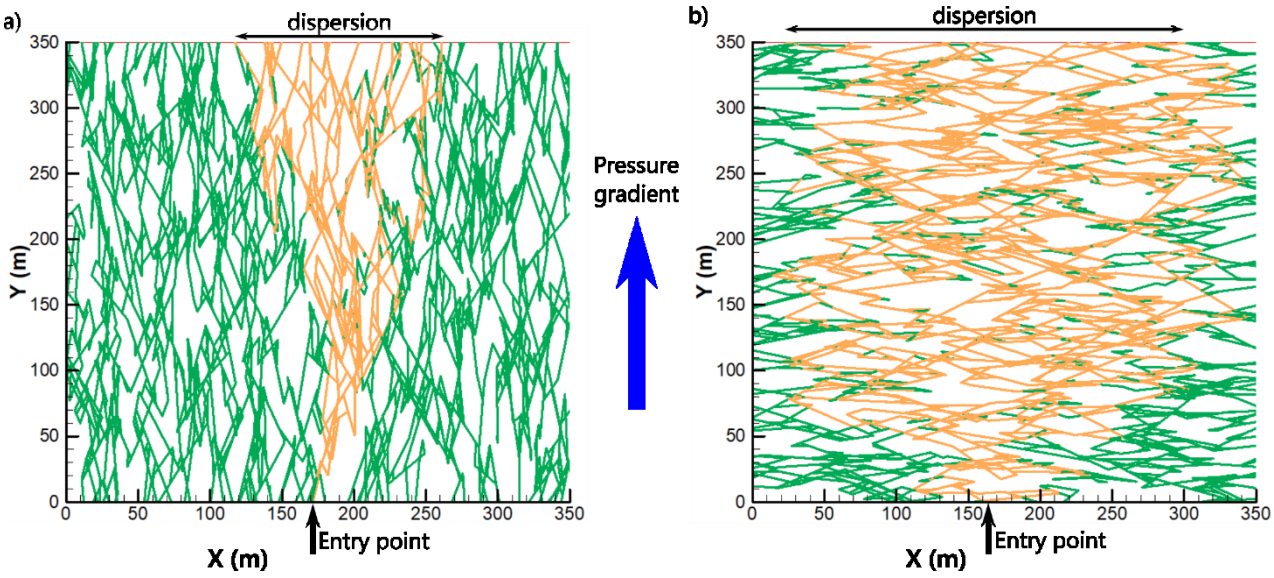

Figure 7. Fluid dispersion in two directions through a DFN realisation of model 2, with a normal dip distribution with standard deviation of 15°. a) Mean fracture dip direction aligned with the pressure gradient. b) Mean fracture dip direction perpendicular to the pressure gradient. The network in b) is identical to that in a) but rotated by 90°.

4. DISCUSSION

4.1 Choice of probability distribution for fracture dip angles

The statistical analysis of fracture dip magnitude and direction presented in Massiot et al. (2017a) yielded up to four fracture sets, with some variations within and between the three wells drilled in various parts of the field (see also McNamara et al., 2015). Some of the fractures sets were more present in some boreholes than others, and the resulting orientations are likely not all present in similar quantities across the reservoir. Hence, using synthetic distributions of orientation allows for varying the proportion of each fracture set across a reservoir. This also allows for relating the various fracture orientation populations to a tectonic origin, and to a higher or lower permeability. Indeed, fracture sets of a specific orientation may

1. have been initiated under the current stress regime, or critically stressed under the current stress regime, and likely to conduct fluid flow (Barton et al., 1995; Morris et al., 1996; Jolie et al., 2016; Finnila et al., 2017);
2. be veins closed to fluids, e.g., if they were inherited from a different stress regime and deformation event; or if they have been filled by hydrothermal minerals;
3. be partially open with some potential for reactivation

At Rotokawa, there was no clear correlation between specific fracture sets and permeability (McNamara et al., 2015), though further data acquisition may help clarify this relationship.

The fluid flows calculated from the data-driven model 6 are statistically closest to those made with models with single- (model 2) and double- fracture (model 4) populations. For flow calculations through a fractured reservoir like Rotokawa, we therefore recommend using either (a) a single, single-parameter, normal distribution with σ=15° (model 2), (b) a double-population model with a small (5%) component of fractures inclined by 30° to the dominant population (model 4) or (c) the probability density function derived directly from the borehole data (model 6). However, the dispersion of fluid is higher for the data-based model 6 compared to models 2 and 4, most likely because of the presence of gently-dipping fractures (dipping <50° or > 130°) which, even if rare, increase the amount of dispersion the fracture network produces.

The various models used in this study allow us to investigate the large influence that orientation has on fluid flow and dispersion properties of the reservoir. As additional data is collected, it will allow for associating various permeabilities (e.g. via the aperture parameter) to populations of different orientation. Another approach could be to vary the aperture factor β as a function of stress to reflect the slip and dilation tendencies (Barton et al., 2013; Jolie et al., 2016).

4.2 The role of the 96% of fractures not part of the backbone

In this study, >95% of fractures were found to not directly contribute to permeability and fluid dispersion because they are not connected to the backbone at reservoir scale. These fractures have however other effects on the rock mass: they provide fluid and heat storage, in addition to the matrix; heat transfer, as the thermal conductivity coefficient is different for trapped fluids and rock; they can locally affect the stress field (Kissling et al., 2015); and they can weaken the rock, by having multiple discontinuities present through the rock mass. Indeed, laboratory testing of samples from the Rotokawa reservoir showed that increasing porosity (or microfracture density) correlates well to a decreasing uniaxial compressive strength, increasing permeability, and a decreasing compressional wave velocity (Siratovich et al., 2014, 2016). The pervasive presence of non-connected fractures and their effects on rock properties are important for reservoir management and fracture stimulations worldwide (e.g., Kneafsey et al., 2019; Mafucci et al., 2015).

4.3 Reservoir scale permeability and continuum modelling

Continuum modelling for geothermal reservoir engineering typically uses integrated finite-difference codes, for example TOUGH2 (Pruess, 1991) and Waiwera (e.g. Croucher et al., 2018) to model heat and mass flow in a geothermal reservoir. The models often treat geological units as homogeneous porous media with fixed rock properties and generally do not include fracture flow explicitly, despite these geological units being known to be highly fractured and inhomogeneous. This section offers some thoughts on how continuum models might be populated with rock properties more appropriate to fractured geological units using results similar to those presented in this paper.

At Rotokawa, fracture characteristics of the andesitic reservoir were directly sampled by downhole borehole image logs at three locations and yet, while yielding comparable average linear fracture densities the probability distributions of dip angle are quite distinct at each site, indicating separate fracture populations (Massiot et al., 2017a). Fracture density and orientation also vary locally within boreholes (McNamara et al., 2015). Further, the density of fracturing at Rotokawa is known through numerical geometric modelling to be highly variable, with regions both devoid of fracturing and with higher than average fracturing on length scales of less than ~100 m (Kissling and Massiot, 2017). It is desirable that any equivalent continuum model should faithfully represent this property of the fracture networks, suggesting that minimum element sizes should be such that this length scale can be resolved.

Of the fractured rock properties derived in this paper, hydrodynamic fluid dispersion is the only one that it is not generally included in geothermal reservoir models. This paper has demonstrated that this is a significant process in the Rotokawa andesites and it should therefore be included in continuum modelling. Fluid dispersion is also key in assessing heat sweeping of the rock mass by conduction, which is key to successful strategies for re-injection and enhanced geothermal systems. To represent fluid dispersion in a continuum geothermal reservoir model, a hydrodynamic dispersion term (e.g. Neretnieks., 1983; Schwartz and Smith, 1988) must be added to the fluid and heat transport equations that are solved by the geothermal simulation code.

Including permeability and dispersion properties of fractured rock into continuum models of geothermal reservoirs could be achieved through (a) generation of probability density functions (PDF) of permeability (across- and along-dip), permeability anisotropy, and fluid dispersion in models presented in this paper, (b) assignment of these properties following the PDFs on an element by element basis and (c) calibration of the model with reservoir data and use of multiple model realisations to quantify model variability and uncertainties. The property estimates presented in this paper are necessarily crude because they are based on only a small number of simulations (10 for each model), but by carrying out larger numbers of simulations (perhaps ~1000 or more) more robust probability density functions (PDFs) of these properties can be derived. This scheme is computationally more intensive than the normal practice of using a single set of rock properties, but this cost would be outweighed by the benefits obtained by including an additional and important physical process into the modelling.

5. CONCLUSIONS

We have presented seven different models for studying the effects of fracture dip on the hydraulic behavior of the Rotokawa andesites, based on fracture dip magnitudes measured *in-situ*. Individual models consist of probability distributions for fracture length, fracture location within the model and fracture orientation. We calculate flows across 'reservoir-scale' regions populated with fractures generated using these distributions. Flow calculations are performed using a 'cubic flow' law and are both isothermal and steady state. Models are used to explore the variability of the permeability (in two directions), the permeability anisotropy and the tendency of the fracture networks to disperse fluid. The fracture models demonstrate that large fluid dispersion occurs at reservoir scale.

A uniform distribution for dip angles is unrealistic for Rotokawa, but the calculated permeability anisotropy for this network is consistent with the expected value of one (within statistical uncertainties) which provides a valuable confirmation for our methods. A model with normally distributed dip angles and a low standard deviation of 6° is generally unable to provide continuous connectivity perpendicular to the mean fracture direction. In contrast, models with larger standard deviations, or with additional populations with different mean/standard deviation will provide good permeability both along-dip and across-dip. All models are found to disperse fluid, and the magnitude of this effect is inversely related to the permeability anisotropy of the network.

For the Rotokawa andesites, three of the seven fracture population models appear to be suitable for further investigation. These are a 'data-driven' model, a two sub-population model and, most simply, a single normal distribution with a moderate standard deviation. Other models, for example with three populations of fractures or single-distribution models with higher standard deviation do not appear to offer any advantage over these. Ultimately our aim is to use these fracture population models to inform more traditional continuum models of the Rotokawa geothermal system, with the hope that they will provide a better description of fluid flow within the reservoir and aid the responsible and sustainable use of that resource in the future.

ACKNOWLEDGEMENTS

This project is funded by the New Zealand Ministry of Business, Innovation and Employment through the GNS Science-led research programme Empowering Geothermal Energy (contract C05X1706).

REFERENCES

Barton, C. A., Zoback, M. D., and Moos, D.: Fluid flow along potentially active faults in crystalline rock. *Geology*, 23(8), (1995), 683–686. doi: 10.1130/0091-7613(1995)023<0683:FFAPAF>2.3.CO;2.

Barton, C. A., Moos, D., Hartley, L., Baxter, S., Foulquier, L., Holl, H., and Hogarth, R.: Geomechanically coupled simulation of flow in fractured reservoirs. Proceedings of the 38th Workshop on Geothermal Engineering, Stanford (2013).

Bignall, G., Rae, A. J., and Rosenberg, M. D.: Rationale for targeting fault versus formation-hosted permeability in high-temperature geothermal systems of the Taupo Volcanic Zone, New Zealand. Proceedings of the World Geothermal Congress (2010).

Bonnet, E., Bour, O., Odling, N. E., Davy, P., Main, I., Cowie, P. A., and Berkowitz, B.: Scaling of fracture systems in geological media. *Reviews of Geophysics*, **39**(3), (2001), 347–383. doi: 10.1029/1999RG000074.

Boussinesq, J.: Memoire sur l'influences des frottements dans les movements reguliers des fluids. *Journal de Mathématiques Pures et Appliqués*, 13, (1868), 377-424.

Cheng, Q., Wang, X., and Ghassemi, A.: Numerical simulation of reservoir stimulation with reference to the Newberry EGS. *Geothermics*, 77, (2019), 327–343. doi: 10.1016/j.geothermics.2018.09.011.

Croucher, A., O'Sullivan, J., Yeh, A., and O'Sullivan, M.: Benchmarking and experiments with Waiwera, a new geothermal simulator. Proceedings 43rd Workshop on Geothermal Reservoir Engineering, Stanford University (2018).

Davatzes, N. C., and Hickman, S.: Stress, fracture, and fluid-flow analysis using acoustic and electrical image logs in hot fractured granites of the Coso Geothermal Field, California, U.S.A. In M. Poppelreiter, C. Garcia-Carballido, and M. Kraaijveld (Eds.), Dipmeter and borehole image log technology: AAPG Memoir 92 (pp. 259–293), (2010). doi:10.1306/13181288M923134.

Jolie, E., Klinkmueller, M., Moeck, I., and Bruhn, D.: Linking gas fluxes at Earth's surface with fracture zones in an active geothermal field. *Geology*, 44(3), (2016), 187–190. doi: 10.1130/G37412.1.

Kneafsey, T. J., Blankenship, D., Knox, H. A., Johnson, T. C., Ajo-Franklin, J., Schwering, P. C., Dobson, P.F., Morris, J., White, M., Podgorney, R., Roggenthen, W., Doe, T., Mattson, E., Valladao, C., and EGS Collab Team.: EGS Collab Project: Status and Progress. Proceedings 44th Workshop on Geothermal Reservoir Engineering, Stanford University (2019).

Kissling, W. M., Ellis, S.E., McNamara, D.D. and Massiot, C.: Modelling fluid flow through fractured rock: Examples using TVZ Geothermal Reservoirs. Proceedings 37th New Zealand Geothermal Workshop (2015).

Kissling, W. M. and Massiot, C.: Geometric modelling of fracture networks in an Andesite-hosted geothermal reservoir. Proceedings 39th New Zealand Geothermal Workshop (2017).

Kissling, W. M. and Massiot, C.: Modelling flows in discrete fracture networks derived from a New Zealand lava-hosted geothermal system. Proceedings 40th New Zealand Geothermal Workshop (2018).

Klimczak, C., Schultz, R. A., Parashar, R., and Reeves, D. M.: Cubic law with aperture-length correlation: implications for network scale fluid flow. *Hydrogeology Journal*, 18(4), (2010), 851–862. doi: .1007/s10040-009-0572-6.

Liu, R., Li, B, Jiang, Y.: Critical hydraulic gradient for nonlinear flow through rock fracture networks: The role of aperture, surface roughness and number of intersections. *Advances in Water Resources,* 88, (2016), 53-65.

Finnila, A., Doe, T., and Mclaren, R.: Dependency of EGS Development on the Alignment between Natural Fracture Set Orientations and Regional Stress State. Proceedings 42nd Workshop on Geothermal Reservoir Engineering, Stanford University (2017).

Maffucci, R., Bigi, S., Corrado, S., Chiodi, A., Di Paolo, L., Giordano, G., and Invernizzi, C.: Quality assessment of reservoirs by means of outcrop data and "discrete fracture network" models: The case history of Rosario de La Frontera (NW Argentina) geothermal system. *Tectonophysics*, 647–648, (2015), 112–131. Doi: 10.1016/j.tecto.2015.02.016.

Masri, A., Barton, C. A., Hartley, L., and Ramadhan, Y.: Structural Permeability Assessment Using Geological Structural Model Integrated with 3D Geomechanical Study and Discrete Facture Network Model in Wayang Windu Geothermal. Proceedings of the 40th Workshop on Geothermal Reservoir Engineering, Stanford, (2015).

Massiot, C., McNamara, D.D., Lewis, B.: Interpretive review of the acoustic borehole image logs acquired to date in the Wairakei-Tauhara Geothermal Field. GNS Science report 2013/04. p. 26. (2013).

Massiot, C., McNamara, D.D., and Lewis, B.: Processing and analysis of high temperature geothermal acoustic borehole image logs in the Taupo Volcanic Zone, New Zealand. *Geothermics*, 53, (2015), 190-201. doi: 10.1016/j.geothermics.2014.05.0107.

Massiot, C.; Townend, J.; Nicol, A.; McNamara, D.D.: Statistical methods of fracture characterisation using acoustic borehole televiewer log interpretation. *Journal of Geophysical Research*, 122(8), (2017a), 6836-6852. doi: 10.1002/2017JB014115.

Massiot, C., McLean, K., McNamara, D. D., Sepulveda, F., and Milicich, S. D.: Discussion Between a Reservoir Engineer and a Geologist: Permeability Identification from Completion Test Data and Borehole Image Logs Integration. Proceedings 39th New Zealand Geothermal Workshop (2017b).

McNamara, D. D., Sewell, S. M., Buscarlet, E., and Wallis, I. C.: A review of the Rotokawa Geothermal Field, New Zealand. *Geothermics*, 59(B), (2016), 281–293. doi: 10.1016/j.geothermics.2015.07.007.

McNamara, D.D., Massiot, C., Milicich, S.M.: Characterizing the subsurface structure and stress of new Zealand's geothermal fields using borehole images. *Energy Procedia*, 125, (2017), 273-282.

Milicich, S. D., Clark, J. P., Wong, C., and Askari, M.: A review of the Kawerau Geothermal Field, New Zealand. *Geothermics*, 59, (2016), 252–265. doi: 10.1016/j.geothermics.2015.06.012.

Morris, A., Ferrill, D.A., Henderson, D.B.: Slip-tendency analysis and fault reactivation. *Geology*, 24(3), (1996), 275-278.

Neretnieks, I.: A note on Fracture Flow Dispersion Mechanisms in the Ground. *Water Resources Research*, 19/2, (1983), 364–370.

Pruess, K.: TOUGH2 – A General-Purpose Numerical Simulator for Multiphase Fluid and Heat Flow. Lawrence Berkeley Laboratory Report LBL-29400. (1991).

Siratovich, P., Heap, M. J., Villeneuve, M. C., Cole, J. W., and Reuschle, T.: Physical property relationships of the Rotokawa Andesite, a significant geothermal reservoir rock in the Taupo Volcanic Zone, New Zealand. *Geothermal Energy*, 2(10), (2014). doi: 10.1186/s40517-014-0010-4.

Siratovich, P., Heap, M. J., Villeneuve, M. C., Cole, J. W., and Kennedy, B. M.: Mechanical behaviour of the Rotokawa Andesites (New Zealand): Insight into permeability evolution and stress-induced behaviour in an actively utilised geothermal reservoir. *Geothermics*, 64(6), (2016), 897–905. doi: 10.1007/s13398-014-0173-7.2.

Stimac, J., Nordquist, G., Suminar, A., and Sirad-Azwar, L.: An overview of the Awibengkok geothermal system, Indonesia. *Geothermics*, 37, (2008), 300–331. doi: 10.1016/j.geothermics.2008.04.004.

Schwartz, F.W. and Smith, L.: A Continuum Approach for Modeling Mass Transport in Fractured Media. *Water Resources Research*, 24/8, (1988), 1360-1372.

Terzaghi, R. D.: Sources of error in joint surveys. *Geotechnique*, 15(3), (1965), 287–304. doi: 10.1680/geot.1965.15.3.287.

Villamor, P., Berryman, K. R., Ellis, S. E., Schreurs, G., Wallace, L. M., Leonard, G. S., Langridge, R.M. and Ries, W. F.: Rapid evolution of subduction-related continental intra-arc rifts: The Taupo Rift, New Zealand. *Tectonics*, 36, (2017a), 2250-2272.

Villamor, P., Nicol, A., Seebeck, H. C., Rowland, J. V., Townsend, D., Massiot, C., McNamara, D.D., Milicich, S.D. and Alcaraz, S.: Tectonic structure and permeability in the Taupō rift: New insights from analysis of Lidar derived DEMs. Proceedings 39th New Zealand Geothermal Workshop (2017b).

Wilson, C. J. N., and Rowland, J. V.: The volcanic, magmatic and tectonic setting of the Taupo Volcanic Zone, New Zealand, reviewed from a geothermal perspective. *Geothermics*, 59, (2016), 1–20. doi:10.1016/j.geothermics.2015.06.01.

Wood, C. P., Brathwaite, R. L., and Rosenberg, M. D.: Basement structure, lithology and permeability at Kawerau and Ohaaki geothermal fields, New Zealand. *Geothermics*, 30(4), (2001), 461–481. doi: 10.1016/S0375-6505(01)00003-7.

Zimmerman, R.W. and Bodvarsson, G.S.: Hydraulic Conductivity of Rock Fractures. Lawrence Berkeley Laboratory Report LBL-35976. (1994).